Published in final edited form as:
IEEE Trans Biomed Eng. 2011 August ; 58(8): . doi:10.1109/TBME.2011.2152839.

Eigendecomposition-Based Clutter Filtering Technique for Optical Micro-Angiography

Siavash Yousefi,
Electrical Engineering Department, University of Washington, Seattle, WA 98195 USA

Zhongwei Zhi, and
Bioengineering Department, Univertsity of Washington, Seattle, WA 98195 USA

Ruikang K. Wang*
Department of Bioengineering, University of Washington, Seattle, WA 98195

Siavash Yousefi: siavash@uw.edu; Zhongwei Zhi: zhizhongweihust@gmail.com

Abstract

In this paper, we propose eigendecposition- (ED-) based clutter filtering technique for 3D optical imaging of blood flow. Due to its best mean square approximation of the clutter, eigen-regression filters can theoretically provide maximum clutter suppression. Compared to the existing clutter rejection techniques in the literature used for optical imaging of blood flow, ED-based clutter filtering is less sensitive to tissue motion and can efficiently suppress the clutter while preserving the flow information. Therefore, it creates images with better contrast in the presence of bulk motion. The performance of the proposed ED-based technique is compared with that of phase compensation method and static high-pass filtering. The quantitative and qualitative performances are compared with each other in phantom studies and in vivo imaging, respectively. Also, 3D image of microvascular structures in mouse ear is presented where the clutter has been suppressed with ED-based technique. This technique can be used in applications where involuntary movements due to cardiac and respiratory cycles are inevitable (such as retinal imaging).

Index Terms

Fourier domain optical coherence tomography (FDOCT); clutter rejection filters; eigen-regression filters; optical microangiography (OMAG)

I. Introduction

Since it was first reported in early 1990s [1] optical coherence tomography (OCT) has been widely used to non-invasively provide high resolution, depth resolved cross-sectional and three-dimensional (3-D) images of highly scattering samples [2, 3]. More recently, spectral-domain OCT (SDOCT) and swept-source OCT (SSOCT) imaging have been developed where these frequency-domain OCT (FDOCT) methods have advantages over time-domain ones in terms of acquisition speed, sensitivity and signal to noise ratio [4, 5]. In order to compensate for the complex conjugate ambiguity and acquisition speed which limited the practical applications of FDOCT, real-time *in vivo* full-range complex FDOCT has been developed to increase the ranging distance in the sample [6, 7].

*wangrk@u.washington.edu; phone: 206-616-5025; fax: 206-685-3300.

There are various methods reported in the literature to visualize blood flow in vessels and contrast them from surrounding tissue microstructures using OCT imaging systems. Some methods utilize the Doppler shift in the phase information of OCT images for optical flow measurement [8–18] while some statistical methods analyze the variations of speckle in the OCT structural images [19–21].

Optical Doppler tomography (ODT) combines Doppler velocimetry with OCT and utilizes the Doppler shift in the frequency of light scattered from a moving particle (such as red blood cells) to measure the velocity both in time-domain [8] and frequency-domain [9] OCT. In order to detect the Doppler shifts in the frequency spectrum, multiple observations (ensembles) of the interference signal from the same location are acquired. Then, the Doppler center frequency is estimated using spectrogram method based on the short-time Fourier transform (STFT) algorithm. However, the minimum detectable Doppler frequency shift varies inversely with the FFT window time at each pixel, which introduces a trade-off between velocity sensitivity and imaging speed as well as spatial resolution [10].

In order to remove the relationship between the velocity sensitivity and spatial resolution while maintaining a high acquisition speed, phase resolved optical Doppler tomography (PRODT) was introduced in time [10] and frequency domain [9]. PRODT evaluates the phase difference between adjacent A-lines within one B-image to estimate the Doppler frequency shift. Then, the estimated mean frequency is used to measure the blood flow velocity using Kasai autocorrelation technique [11]. Although widely used, the sensitivity of PRODT to blood flow is low and makes it difficult to visualize 3D microcirculations in applications such as human skin where the blood flow within the capillary vessels is in the order of 0.1–0.9 mm/s [12]. Also, it would be advantageous to extract Doppler information using the frequency domain method because the velocity dynamic range of a phase-resolved ODT system is determined by A-line scanning rate. The drawbacks of Doppler OCT are its insensitivity to transverse component of blood flow and also its dependence on the phase stability of the system.

Vokac et al. [13] proposed a method to improve the sensitivity of PROCT by utilizing the phase variance between adjacent B-scans. However, their method was sensitive to slow flows within capillary vessels, because, the time interval between the adjacent B-scan images was relatively long (~ few microseconds). Because of the relatively long imaging time (~25 min), their method could not be used for *in vivo* human applications such as human skin or retina where involuntary subject movements are inevitable.

Optical micro-angiography (OMAG) is a three dimensional imaging modality [14] which has shown promising results for imaging cerebral blood flow in mice [15] and rat [16] and ocular blood flow in human retina [17]. OMAG exploited the inherent properties of the OCT signals to efficiently separate the moving and static scattering elements within tissue, hence enabled precise localization of blood perfusion in three-dimensional microstructures. This was achieved by modulating the spatial OCT spectral interferogram at a constant modulation frequency while the probe beam was scanned across the B scans. Also, another extension of OMAG has been used to visualize detailed microcirculation within human skin tissue beds [18]. In that extension, as opposed to the previous OMAG method, the A-line density of B-scan was decreased, while B-scan density was increased. The OMAG algorithm was then applied on C-scan direction (elevation direction), rather than B-scan direction (lateral direction) as in the conventional approach.

Clutter rejection is one of the most important data processing steps in visualizing blood perfusion and vascular structures. Clutter is the scattered signal from stationary or slowly moving tissues in the coherence sampling volume of the probe beam in the sample arm.

Since clutter signal is typically stronger than the Doppler signal, it can reduce the sensitivity and accuracy in estimating the flow. The concept of clutter rejection filtering is similar to medical ultrasonic imaging where mechanical ultrasound waves are used to visualize the blood flow in arteries and veins. Color Doppler imaging (CDI), a tomographic real-time imaging technique, is one of the principal ultrasonic imaging modalities that is similar to optical micro-angiography and has a wide range of clinical applications. In CDI, blood flow of an ROI (region of interest) is color-coded and visualized on top of B-mode (gray-scale coded intensity image of tissue structures) images and displayed in real-time (33 frames per second or higher). In order to estimate the Doppler frequency shift, clutter should be suppressed using a post-processing step commonly known as clutter rejection filtering. Clutter filters can be divided into three main categories: static filters where an IIR or FIR filter with fixed coefficients is used, adaptive filters where the characteristics of the filter is adapted to the received signal, and a combination of static and adaptive filters. Static filters are widely used and preferred over adaptive ones in commercial products because they can be implemented in real-time. However, static filters cannot efficiently remove clutter due to nonstationary tissue motions from cardiac activities, respiration and the transducer/patient movements. Also, the assumption that clutter is centered around zero frequency is not always met in practice. Several adaptive filters have been proposed among which eigen-regression filters can theoretically provide the maximum clutter suppression due to its best mean square approximation of the clutter [19].

There are several methods proposed in the literature for clutter rejection in OCT-based flow imaging. Ren and Li [23] developed a delay line filter (DLF) to reject the clutter effect and showed that a first-order phase-shifted DLF could effectively remove the clutter in capillary flow phantom and in mouse ear. Compared to the conventional phase-resolved optical Doppler tomography, DLF was more sensitive to Doppler flow and picking up small blood vessels that were masked by clutter signal in PR-OCT. Also An and Wang [18] applied a static high-pass filter in OMAG to remove the clutter component from the received Doppler signal. However, these static filters were sensitive to tissue movements and their performance in removing the clutter degraded at the presence of unwanted motion. In order to compensate bulk tissue motion, An and Wang [17] proposed a phase compensation method to estimate clutter's center frequency and shift it to zero, and then applied a static filter to remove the clutter component. However, this technique may not be effective when the clutter is broadband or the flow signal is very strong where the estimated center frequency may not be accurate.

In this paper, we propose eigendecposition-based filtering technique for clutter rejection in optical imaging of blood flow. A series of flow phantom studies are performed where tissue (phantom) motion is externally introduced by tapping over the imaging surface to simulate tissue motion. The performance of ED-based clutter rejection in removing the tissue motion and picking up the flow information is studied and the efficiency of the proposed technique is compared with those of phase-compensation method and static high-pass filtering. Also, *in vivo* experiments are performed for visualizing microcirculations within human skin tissue beds and the performance of different clutter filters is compared with each other. Finally, we show the sensitivity of the ED-based clutter rejection filters in picking up blood flow in the capillaries of mouse ear.

II. Methodology

A. Experimental Set-up

The schematic of the imaging system (UHS-OMAG) is shown in Fig. 1 [18]. The light source was a superluminiscent diod (SLD, DenseLight, Singapore) with the center wavelength of 1310 nm and bandwidth of 65 nm. The axial resolution of the system in the

air using this SLD was ~12 μm. An optical circulator was used to couple the light from the SLD into fiber-based Michelson interferometer. In the reference arm of the interferometer, a stationary mirror was utilized after polarization controller (PC). In the sample arm of the interferometer, an objective lens with 50 mm focal length was used to achieve ~16 μm lateral resolution. Then, a 2×2 optical fiber coupler was utilized to recombine the backscattered light from the sample and the reflected light from the reference mirror. Since the wavelength of the light source is invisible to the human eye, a 633 nm laser diode is used as a guiding beam to locate the imaging position. This reference helps to adjust the sample under the OCT system and image the desired location. The recombined light was then routed to a home-built high-speed spectrometer via the optical circulator. In the design of the spectrometer, a collimator with the focal length of 30 mm and a 14-bit, 1024 pixels InGaAs line scan camera were used. The camera speed was 47000 lines per second and the measured signal to noise ratio was ~105 dB with a light power on the sample at ~3 mW. The spectral resolution of the designed spectrometer was ~0.141 nm that provided a detectable depth range of ~3.0 mm on each side of the zero delay line.

B. Scanning protocol and image reconstruction

3D imaging was achieved by using two galvo-scanners to raster-scan the focused beam spot across the sample, with one scanner for X-direction (lateral) scan, and another for Y-direction (elevational) scan. To achieve ultrahigh sensitive imaging of slow microcirculation, a new scanning protocol and flow reconstruction algorithm was utilized [18]. Each B-scan (x-direction scan) was formed by acquiring 256 A-lines with a spacing of ~ 8 μm (which is of the order of the least sampling distance of 10 μm for the system lateral resolution of 16 μm) between adjacent lines, which covered a total x-direction scan range of ~2 mm.

The camera integrating time was set at 31 μs for imaging, allowing 1 μs for downloading the spectral data from CCD (1024 pixels, A scan) to the host computer via CameraLink™ and a high-speed frame grabber board (PCI 1428, National Instruments, USA). This configuration determined a line scan rate of ~47 KHz for the camera, which corresponds to a theoretical imaging rate of 183 frames per second (fps). However, the images were acquired at 150 fps which is at 80% of the maximum theoretical speed of the camera.

In the y-direction (C-scan direction), we captured 1125 B-scans over 1.5 mm on the tissue, which gave a ~1.3 μm spacing between adjacent B scans, indicating the oversampling of ~ 12 in the C-scan direction. The whole 3D volume data was acquired within 6 s. The schematic of the scanning protocol used in this paper is shown in Fig. 2 where the 3D image is formed by m adjacent B-scan cross-sectional images and each B-image is formed by n A-scan captured signals. Also, each A-scan is a vector containing k_j, $j=1,2,\ldots,p$, where k_j is the wavenumber of the light captured by the jth pixel, j is the pixel number of the line scan CCD camera and $p=1024$.

The interference signal of one B-scan captured by the CCD camera can be expressed by

$$I(t,k_j)=S(t,k_j)\cdot E_R^2+2S(t,k_j)\cdot E_R\int_{-\infty}^{\infty}[(a(z,t)\cdot\cos(2)]k_j n(t)z)dz+2S(t,k_j)\cdot E_R a(z_l)\cdot\cos[2k_j n(t)(z_l-vt)] \quad (1)$$

where $I(t,k_j)$ is the light intensity detected by the jth detector at time t, k_j is the wavenumber, j=1,2, …,1024 is the pixel number of the line scan CCS camera, E_R is the light reflected from the reference mirror, $S(k_j)$ is the spectral density of the light source used at k_j, n is the refractive index of tissue, z is the depth coordinate, $a(z)$ is the amplitude of the backscattered light and z is the depth from which the light back scattered from, v is the velocity of moving blood cells in a blood vessel which is located at depth z_l. In this equation, the self cross-

correlation between the light backscattered from different positions within the sample is neglected because the light backscattered from the sample is relatively weaker than the light reflected from the reference mirror. The first term in (1) is the DC signal produced the light reflected from the reference mirror. The second term is the spatial frequency component of the static tissue sample which can provide static structural information of the sample. The third term is the Doppler beating signal which is introduced by the moving particles in the tissue sample.

C. Flow Sensitivity

The maximum detectable velocity that is not phase-wrapped is determined by the time spacing (ΔT) between adjacent A scans, $v = \lambda/2n\Delta T$, where λ is the central wavelength of the light source, n is the average refractive index of the sample and factor of two is accounting for the forward and return path. So, detecting the flow in the capillary, in which the typical flow velocity is ≤100 μm/s, requires the time spacing to be larger than ~4.7 ms which corresponds to a scanning speed of ~213 A scans per second. However, such a long imaging time is not practical for 3D *in vivo* imaging of capillary blood flows. In contrast to the conventional OMAG method, current scanning protocol utilizes scanning in the C-scan direction to increase the sensitivity of the system to the minimum detectable flow while keeping the imaging speed high. In our system setup, the imaging rate is 150 fps (t_C ~6.6 ms). Therefore, considering that the C scan direction is densely sampled at an oversampling factor of 12, the detectable flow velocity would be ~70.8 μm/s while the imaging speed is still kept at 47,000 A scans per second. This detectable flow velocity would be sufficient to image the blood flow in capillaries. It should be noted that the maximum detectable velocity by the system is determined by the system imaging speed. In this case, the imaging speed is the A-scan rate which is 47 KHz and the maximum detectable velocity by the system is ~15 mm/s. However, if the velocity is >70.8 μm/s, the phase wrapping effect will occur and the true velocity may not be measured unless some phase-unwrapping algorithm be used [24]. On the other hand, the minimum detectable flow velocity is determined by the system phase noise floor, $\sigma_{\Delta\phi}{}^2=1/S$ where S is the intensity signal to noise ratio [25]. Thus, with the system signal to noise ratio at 105 dB, the minimum detectable flow velocity would be ~4.0 μm/s.

D. ED-Filtering Formulation

In order to retrieve the flow information, multiple A-lines are acquired from the same location. After removing the DC component in Eq. 1, the phase difference at each depth location is utilized to estimate its corresponding average flow velocity. The received backscattered signal at a particular depth along each A-line form a vector defined as

$$X=[x(1),\ x(2),\ldots,x(N)]^T \quad (2)$$

where N is the ensemble size. The observation or ensemble of samples from one particular depth location is modeled as the sum of three independent zero-mean complex Gaussian processes: a clutter component c, a blood component b and additive white noise n. Its vector notation is given by

$$X=c+b+n \quad (3)$$

ED-based filtering takes advantage of the characteristics unique to high-frequency blood flow mapping that tissue motion is correlated over the depth of interest and the reasonable tissue motion velocities are small but on the same order of the blood flow velocity [22].

Since X is Gaussian, it is completely characterized by its correlation matrix Rx, given by

$$R_x = R_c + R_b + \sigma_n^2 I \quad (4)$$

where R_C is the clutter correlation matrix, R_b is the blood correlation matrix, σ_n^2 is the noise variance, and I is the identity matrix.

Assuming that clutter is the dominant signal and its characteristics are similar along the depth [26], spatial average of the correlation of the received signal along the axial direction is an estimate of the clutter correlation matrix R_C given by

$$\widehat{R}_c = \frac{1}{M}\sum_{i=1}^{M} \widehat{R}_c = \frac{1}{M}\sum_{i=1}^{M} X_i X_i^H \quad (5)$$

where X_i is the complex Doppler signal from depth i, $(.)^H$ is the Hermitian transpose. The estimated correlation matrix $\hat{R}_c$ is decomposed into its corresponding eigenvalues and eigenvectors given by

$$\widehat{R}_c = E \Lambda E^H \quad (6)$$

where $E=[e_1, e_2, \ldots, e_N]$ is the $N \times N$ unitary matrix of eigenvectors, $\Lambda = diag\{\lambda_1, \lambda_2, \ldots, \lambda_N\}$ is the $N \times N$ diagonal matrix of eigenvalues and $\lambda_1 \geq \lambda_2 \geq \ldots \lambda_N = \sigma_n^2$ and σ_n^2 is the noise variance. Assuming that the clutter space is spanned by K eigenvectors, eigenregression filter is applied to the received signal by removing the clutter components as follows

$$Y = (I - \sum_i e_i e_i^H) \cdot X \quad (7)$$

where Y is the Doppler signal after removing the clutter component. Also, the corresponding frequency response of this filter can be represented by

$$H(\omega) = 1 - \frac{1}{N}\sum_i |DTFT\{e_i\}|^2 \quad (8)$$

where DTFT is the discrete-time Fourier transform (DTFT).

And finally, the Doppler center frequency of the flow is estimated by

$$\widehat{f_b} = \frac{1}{2\pi}\tan\left(\frac{Im\{\widehat{R}_y(1)\}}{Re\{\widehat{R}_y(1)\}}\right) \quad (9)$$

where $\hat{R}_y(1)$ is the first lag autocorrelation of Y.

III. Experimental results

We applied the ED-based technique both in phantom and in *in vivo* and compared its quantitative and qualitative performance with that of phase-compensation and high-pass

filtering. Then, we applied ED-based technique to visualize microcirculation in microvascular structures in mouse ear.

A. Phantom studies

First, we performed a series of experiments on a custom-made flow phantom. The phantom was made from gelatin mixed with 2% milk to simulate the background optical heterogeneity of the tissue in which a capillary tube with an inner diameter of ~200 μm was submerged and 2% TiO2 particle solution was flowing in it. The inclining angle of the tube towards the incident beam (Doppler angle) was set at ~80°. The flow rate of the particle was controlled by a precision syringe pump to a range that falls within the detectable range of the OMAG system. In this experiment, the ensemble size of OMAG data was 9. In order to mimic tissue movements, we intentionally introduced motion to the phantom by tapping over the imaging surface and phantom while increasing the tapping intensity for each experiment.

The performance of each clutter filter was measured by two quantities: clutter suppression level (CSL) and flow suppression level (FSL). CSL and FSL are defined by the ratios of the signal power before and after clutter suppression in the already known flow and stationary areas. The comparison criteria are based on the ability of each filter in suppressing the clutter in the stationary areas and the suppression level in the flow area.

Typical performance of different clutter rejection filters for one cross section of the flow phantom is displayed in Fig. 3(A), (B) and (C), where static high-pass filter, phase compensation and ED-based technique have been applied, respectively. In this figure, the darker intensities correspond to less power suppression. Also, the structure image of the phantom is shown in Fig. 3(D) where the flow pipe is located in the center and is surrounded by the phantom material. The structure image is very blurry which shows some motion in the phantom tissue and pipe due to the external motion introduced by tapping. It can be observed that the performance of static high-pass filter is inferior compared to the other two methods. Also, ED-based techniques is superior to the phase compensation method where the pipe's surrounding tissues is brighter (higher suppression level in stationary area). Also, the boundaries of the flow pipe and the edges of the phantom are darker in phase compensation (less suppression of the stationary tissue boundaries) where these areas have been more effectively suppressed via ED.

Table 1 represents the quantitative comparison between different filters where the average FSL and CSL are measured for all experiments. Compared to the other two methods, ED-based technique was more effective in suppressing clutter while its flow suppression was similar to phase compensation. Although static high-pass filter had lower FSL value, it was not as effective as the other two methods in suppressing clutter.

B. Tests on in vivo: Human skin

We applied different clutter filtering techniques to OCT images acquired from human skin. The images were acquired from the back of the finger of a healthy volunteer. In this experiment, the ensemble size of OMAG data was 4. Fig. 4 shows one slice of the 3D image in the X-Y plane which is visualizing microcirculations in reticular dermis (RD) layer of the skin. The RD is the lower layer of the dermis, found under the papillary dermis (PD), composed of thick, densely packed collagen fibers, and the primary location of dermal elastic fibers [27].

Figs. 4(A), (B) and (C) correspond to static high-pass filter, phase compensation and ED-based technique, respectively, applied to the same dataset acquired from the RD layer. It can be observed that ED-based technique, compared to the phase compensation and static high-

pass filter, reveals more detail in the microcirculation and is less sensitive to unwanted tissue motion during optical scanning. Also, when ED-based technique is used, large vessels appear brighter which means that the flow signal is stronger at that location and the flow map image has a better contrast. Note the arrows pointing to the locations where ED-based technique in particular outperforms the other methods and the micro-vascular structure in the pointed locations are distinctively visible in Fig. 4(C) while such structures were not visible in Figs. 4(A) and (B). The estimated root-mean-square (RMS) contrast values of the cross-sectional images shown in Fig. 4(A), (B) and (C) are 41.76, 42.57 and 46.72, respectively.

The RMS contrast is defined as the standard deviation of the pixel intensities and is calculated by

$$Contrast_{RMS} = \sqrt{\frac{1}{MN}\sum_{i=0}^{N-1}\sum_{j=0}^{M-1}(I_{i,j} - \bar{I})^2} \quad (10)$$

where $I_{i,j}$ is the i-th j-th element of the two-dimensional image of size M by N and $\bar{I}$ is the average intensity of all pixel values in the image.

Also, Fig. 5 shows micro-vascular structures in the papillary dermis (PD) layer of the human skin acquired from another location on the back of the finger of a healthy volunteer. Similar to Fig. 4, different techniques have been applied to the same data location where ED-based technique outperformed the other two. The pointed arrows, specifically pinpoint some locations where qualitative comparison between the en-face images confirms the ability of ED-based technique in removing clutter and better assessment of micro-vascular structures. The estimated RMS contrast values of the X-Y images shown in Figs. 5(A), (B) and (C) are 44.98, 45.50 and 52.01, respectively.

C. Tests on in vivo: mouse ear

The skin of the hairless mouse ear closely resembles human skin, with the exception of sweat glands. Mouse ear is ~300 μm thick and is composed of two full-thickness layers of skin separated by a thin supporting skeleton of elastic cartilage. The vascular network of the hairless mouse ear normally originates from three pairs of arterioles and venules entering the base of the ear. Four subdivisions (or orders) of blood vessels are noted from the three primary pairs of arterioles and venules (first-order vessels) to the precapillary arterioles and postcapillary venules (fourth-order vessels). The inner diameters of arterioles range from 35 μm in the first-order arterioles to 8–9 μm in the precapillary arterioles while ranging from 50–400 μm for first-order to 8–9 μm for the fourth-order venules. Also, arteriovenous anastomoses (AVA) with intermittent flow (inner diameters ranging from 10- to 12- μm) supply a branching network of capillaries. Most capillary loops are observed around the hair follicle [28].

We acquired noninvasive 3D optical images from the ear skin of a three months old mouse. A healthy C57 BL/6 mouse weighting around 25 gm was used in this study. The experimental protocol was in compliance with the Federal guidelines for care and handling of small rodents and approved by the Institution Animal Care and Use Committee (IACUC) of University of Washington. Fig. 6 shows an *en-face* (x-z) 3D volumetric projection image of the microvascular network in mouse ear where ED-based clutter filter has been applied to the received OMAG data. Detailed organization of the vascular structure of the capillaries, arterioles, venules and arteriovenous anastomosis can be observed.

IV. Discussions

Compared to the static high-pass filtering and phase-compensation method, ED-based technique was less sensitive to tissue motion and could suppress clutter more efficiently. However, it is computationally more expensive than the other two methods. Although, Lovstakken et al. [29] proposed an algorithm for real-time implementation of adaptive ED-based clutter rejection filtering in ultrasound color Doppler imaging (CDI), static filters are still preferred over adaptive ones in real-time applications.

We implemented static high-pass filter, phase-compensation method and ED-based technique in Matlab® and estimated their performance on a personal computer with a six-core 3.4 Ghz processor and 8 GB of memory. Each frame consisted of 256 A-lines, 512 samples per A-line and 9 ensembles. The average processing time for one frame using static high-pass filter, phase-compensation method and ED-based technique was about 1.775, 5.914 and 2.104 seconds, respectively. Therefore, processing a 3D image which has 200 B-lines using ED-based technique can take ~7 minutes.

ED-based technique assumes that the clutter is the most dominant portion of the received signal. However, when a very strong flow (arteries that are considered very large in the scale of OCT imaging) is present, that assumption is no longer true. In this case, the order of the eigenvalues will change and the largest eigenvalues are no longer corresponding to the clutter.

Also, selecting the appropriate number of eigenvectors to represent clutter space is always a challenge. In most of the *in vivo* experiments, the first two eigenvectors were properly representing the clutter space. However, that was not the case in phantom studies and more than two eigenvectors were removed to better reject clutter components (especially when the tapping intensity and manually introduced motion in the phantom increased). In order to account for this problem, an algorithm can be used to estimate the center frequency of each eigenvector and categorize that as either clutter or flow. In addition, the ensemble size can also impact the number of eigenvectors representing each space.

In our phantom experiments, all the techniques had a satisfactory performance when there was not tapping and no external motion was introduced. However, by increasing the tapping intensity, the high-pass filter and phase-compensation techniques were not efficient in suppressing the phantom motion. ED-based technique was more robust, up to some degree of tapping, and had a satisfactory performance in suppressing the motion in the stationary tissue. However, when there was a very large amount of motion, all the methods failed in tissue motion.

Be noted that ensemble size can have an impact on the performance of ED-based technique and increasing the ensemble size will improve the performance of clutter filter in better estimation of the clutter spectrum. However, increasing the ensemble size, linearly reduces the imaging speed and frame rate and there is always a trade-off between ensemble size and imaging speed.

V. Conclusion

In this paper, we proposed ED-based clutter filtering technique for clutter suppression in optical imaging of blood flow. Although eigen-regression filters have already been used in the field of ultrasonography, to our knowledge, this is the first time this method has been used in the field of optical blood flow imaging.

The performance of the proposed filter was compared with two existing methods, static high-pass filtering and phase-compensation method, where ED-based technique outperformed the other two methods, qualitatively and quantitatively. We compared the performance of these filters in a custom-built phantom and *in vivo* human skin. Also, the 3D projection view of *in vivo* imaging of mouse ear using ED-based technique was presented. This technique can be used in flow imaging applications where clutter suppression is required to extract flow information from the stationary or slowly moving tissues and specially when involuntary movements due to cardiac and respiratory cycles are inevitable (such as retina imaging).

Acknowledgments

This work was supported in part by research grants from the National Institute of Health (NIH) (R01HL093140, R01HL093140S and R01EB009682).

The authors would like to thank Mr. Lin An and Ms. Jia Qin for optical system set-up and data acquisition for the mouse ear experiment. This work was supported in part by research grants from the National Institute of Health (NIH) (R01HL093140, R01HL093140S and R01EB009682).

References

1. Huang D, Swanson EA, Lin CP, Schuman JS, Stinson WG, Chang W, Hee MR, Flotte T, Gregory K, Puliafito CA. Optical coherence tomography. Science (New York, NY). 1991; 254(5035):1178.
2. Fercher AF, Drexler W, Hitzenberger CK, Lasser T. Optical coherence tomography-principles and applications. Reports on Progress in Physics. 2003; 66:293–303.
3. Tomlins PH, Wang RK. Theory, developments and applications of optical coherence tomography. Journal of Physics D: Applied Physics. 2005; 38:2519.
4. Leitgeb R, Hitzenberger C, Fercher AF. Performance of fourier domain vs. time domain optical coherence tomography. Optics Express. 2003; 11(8):889–894. [PubMed: 19461802]
5. Choma M, Sarunic M, Yang C, Izatt J. Sensitivity advantage of swept source and Fourier domain optical coherence tomography. Optics Express. 2003; 11(18):2183–2189. [PubMed: 19466106]
6. An L, Subhash HM, Wang RK. Full range complex spectral domain optical coherence tomography for volumetric imaging at 47 000 A-scans per second. Journal of Optics. 2010; 12:84003. [PubMed: 21643509]
7. Wang RK. *In vivo* full-range complex Fourier domain optical coherence tomography. Applied Physics Letters. 2007; 90(5)
8. Chen Z, Milner TE, Dave D, Nelson JS. Optical Doppler tomographic imaging of fluid flow velocity in highly scattering media. Optics Letters. 1997; 22(1):64–66. [PubMed: 18183104]
9. Wang L, Wang Y, Guo S, Zhang J, Bachman M, Li GP, Chen Z. Frequency domain phase-resolved optical Doppler and Doppler variance tomography. Optics Communications. 2004; 242(4–6):345–350.
10. Ding Z, Zhao Y, Ren H, Nelson J, Chen Z. Real-time phase-resolved optical coherence tomography and optical Doppler tomography. Optics Express. 2002; 10(5):236–245. [PubMed: 19436351]
11. Kasai C, Namekawa K, Koyano A, Omoto R. Real-time two-dimensional blood flow imaging using an autocorrelation technique. IEEE Transactions on Sonics and Ultrasonics. 1985; 32(3): 458–464.
12. Kellam K, Altmeyer P. Capillary blood cell velocity in human skin capillaries located perpendicularly to the skin surface: measured by a new laser Doppler anemometer. Microvascular Research. 1996; 52:188–192. [PubMed: 8901447]
13. Vakoc BJ, et al. Three-dimensional microscopy of the tumor microenvironment in vivo using optical frequency domain imaging. Nature Medicine. 2009; 15(10):1219–1223.
14. Wang RK, Jacques SL, Ma Z, Hurst S, Hanson SR, Gruber A. Three dimensional optical angiography. Optics Express. 2007; 15(7):4083–4097. [PubMed: 19532651]

15. Wang RK, Hurst S. Mapping of cerebrovascular blood perfusion in mice with skin and skull intact by Optical Micro-Angiography at 1.3 μm wavelength. Optics Express. 2007; 15(18):11402–11412. [PubMed: 19547498]
16. Wang RK, An L. Doppler optical micro-angiography for volumetric imaging of vascular perfusion *in vivo*. Optics Express. 2009; 17(11):8926–8940. [PubMed: 19466142]
17. An L, Wang RK. In vivo volumetric imaging of vascular perfusion within human retina and choroids with optical micro-angiography. Optics Express. 2008; 16(15):11438–11452. [PubMed: 18648464]
18. An L, Qin J, Wang RK. Ultrahigh sensitive optical microangiography for in vivo imaging of microcirculations within human skin tissue beds. Optics Express. 2010; 18(8):8220–8228. [PubMed: 20588668]
19. Barton J. Flow measurement without phase information in optical coherence tomography images. Optics Express. 2005; 13(14):5234–5239. [PubMed: 19498514]
20. Mariampillai A, Leung MKK, Jarvi M, Standish BA, Lee K, Wilson BC, Vitkin A, Yang VXD. Optimized speckle variance OCT imaging of microvasculature. Optics Letters. 2010; 35(8):1257–1259. [PubMed: 20410985]
21. Sudheendran N, Syed SH, Dickinson ME, Larina IV, Larin KV. Speckle variance OCT imaging of the vasculature in live mammalian embryos. Laser Physics Letters. 2011; 8(3):247–252.
22. Kruse DE, Ferrara KW. A new high resolution color flow system using an eigendecomposition-based adaptive filter for clutter rejection. IEEE Transactions on Ultrasonics, Ferroelectrics and Frequency Control. 2002; 49(10):1384–1399.
23. Li X, Ren H. Clutter rejection filters for optical Doppler tomography. Optics Express. 2006; 14(13):6103–3112. [PubMed: 19516783]
24. Subhash HM, Davila V, Sun H, Nguyen-Huynh AT, Shi X, Nuttall AL, Wang RK. Volumetric in vivo imaging of microvascular perfusion within the intact cochlea in mice using ultra-high sensitive optical microangiography. IEEE Transactions on Medical Imaging. 30(2):224–230. [PubMed: 20813632]
25. Vakoc B, Yun S, de Boer J, Tearney G, Bouma B. Phase-resolved optical frequency domain imaging. Optics Express. 2005; 13(14):5483–5493. [PubMed: 19498543]
26. Song F, Zhang D, Gong X. Performance evaluation of eigendecomposition-based adaptive clutter filter for color flow imaging. Ultrasonics. 2006; 44:e67–71. [PubMed: 16844157]
27. Marks, JG.; Miller, JJ. Lookingbill and Marks' Principles of Dermatology. Saunders Elsevier; 2006.
28. Eriksson E, Boykin JV, Pittman RN. Microvascular Research. 1980; 19(3):374–379. [PubMed: 7382855]
29. Lovstakken L, Bjaerum S, Kristoffersen K, Haaverstad R, Torp H. Real-time adaptive clutter rejection filtering in color flow imaging using power method iterations. IEEE Transactions on Ultrasonics, Ferroelectrics and Frequency Control. 2006; 53(5):1597–1608.

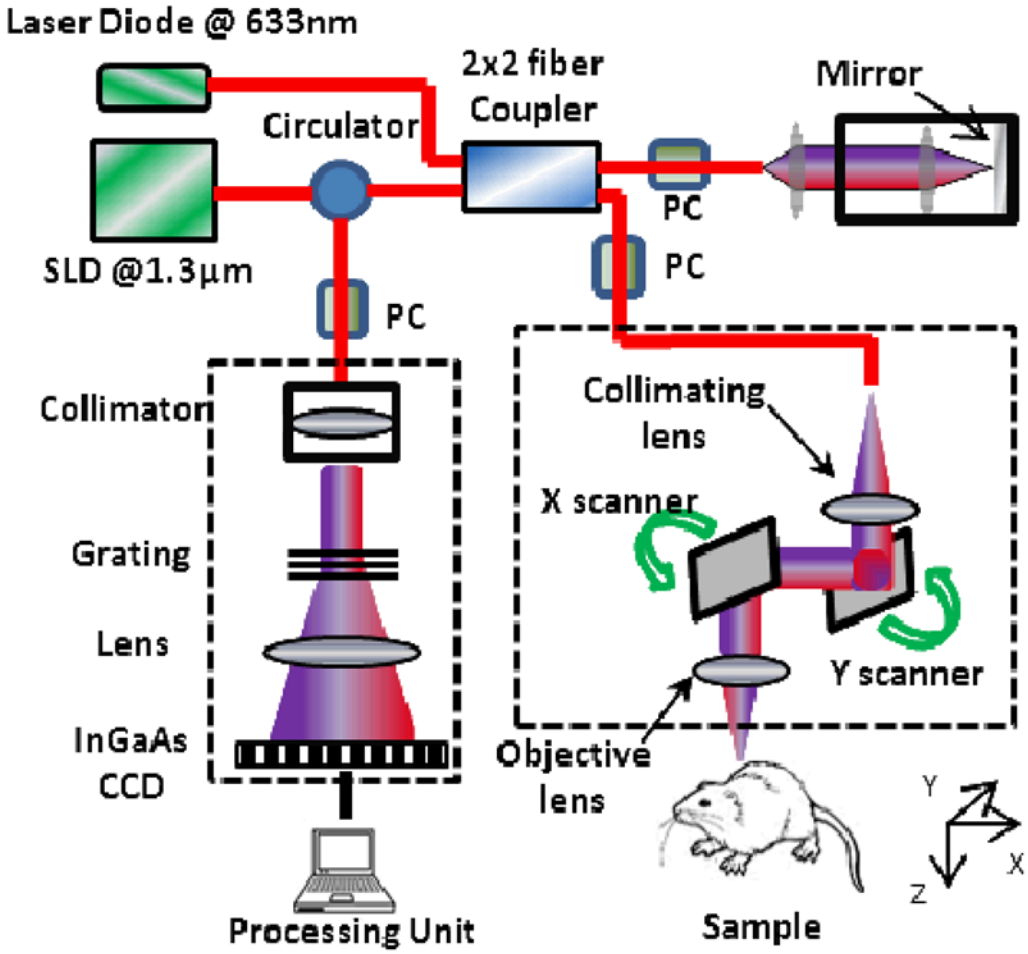

Fig. 1.
Schematic diagram of the imaging system, where PC represents the polarization controller (PC) and CCD is the charged coupled device (camera).

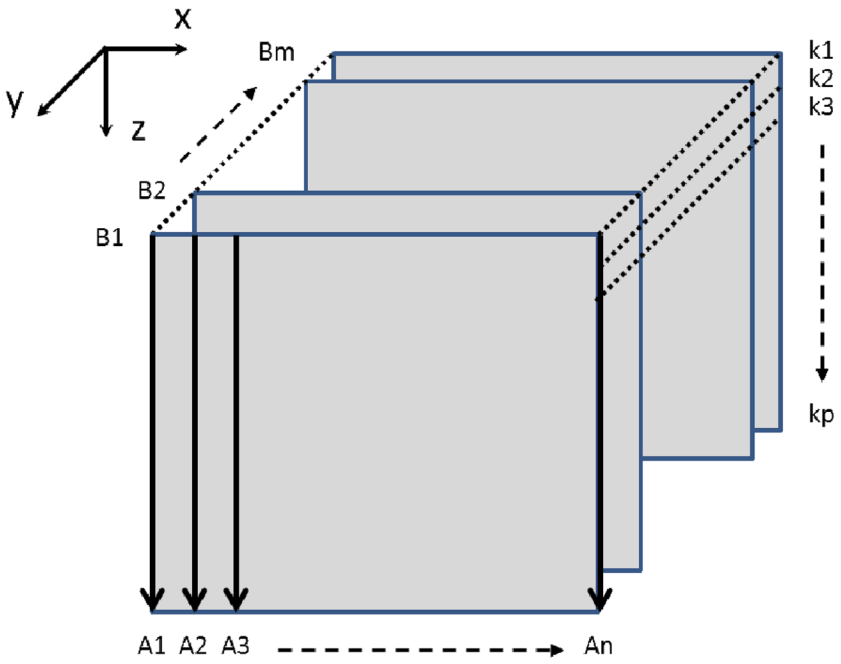

Fig 2.
Schematic of the scanning protocol for 3D imaging.

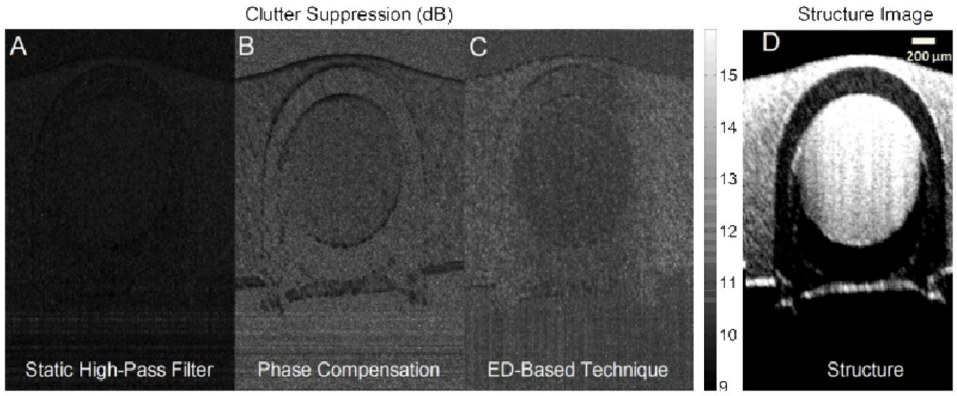

Fig. 3.

Typical performance of clutter rejection filters in flow phantom studies. (A) static high-pass filter, (B) phase compensation and (C) ED-based technique. The flow pipe is located in the center, surrounded by tissue material. The intensity values correspond to the suppression level after clutter rejection. Higher suppression outside the tube (more bright) and lower suppression inside the tube (less bright) is preferred. (D) Structure image, which is blurry because of the motion introduced by tapping over the imaging surface to simulate tissue motion.

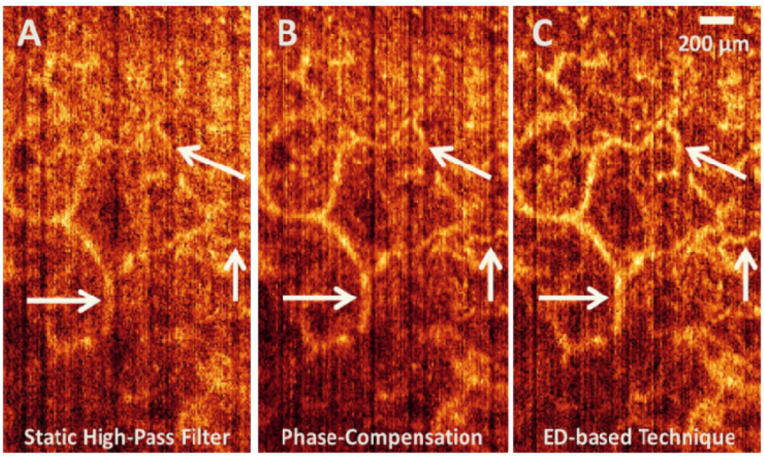

Fig. 4.

Qualitative comparison between static high-pass filter (A), phase compensation (B) and ED-based technique (C) on one slice of the human skin in the X-Y plane showing vascular perfusion in reticular dermis layer. The estimated root-mean-square contrast value for each image is 41.76, 42.57 and 46.72 for Fig. 4(A), (B) and (C), respectively.

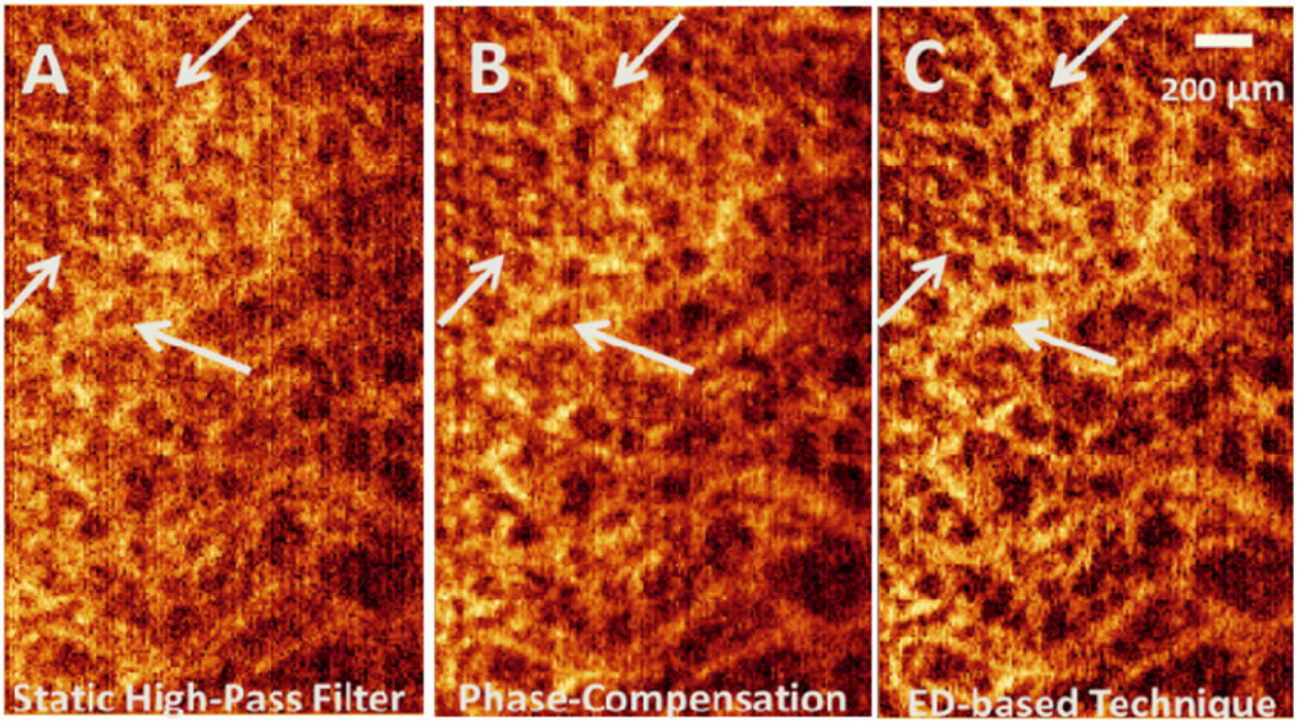

Fig. 5.
Qualitative comparison between static high-pass filter (A), phase compensation (B) and ED-based technique (C) on one slice of the human skin in the X-Y plane showing vascular perfusion in papillary dermis layer. The estimated root-mean-square contrast values are 44.98, 45.50 and 52.01 for Figs. 5. A, B and C, respectively.

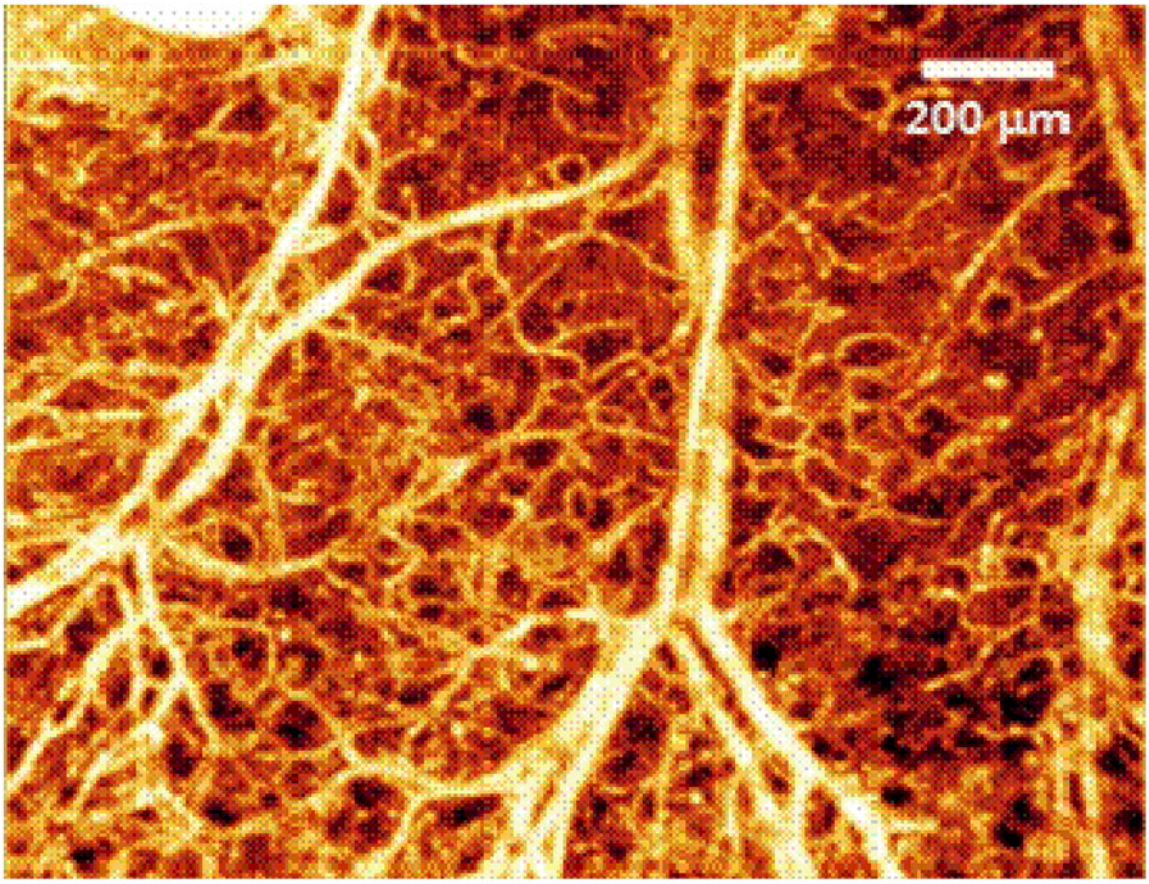

Fig. 6.
En-face 3D volumetric projection image of the microvascular network in mouse ear where ED-based technique has been applied to suppress clutter.

Table 1

Quantitative comparison between different filters in phantom sutides

	Static High-Pass Filter	Phase- Compensation	ED-Based Technique
CSL (dB)	10.7	11.9	12.9
FSL (dB)	9.6	10.7	10.7